Energy loss rate of an electron in three-dimensional tilting Dirac semimetals

Xiaokang Dai and Qinjun Chen[*]

School of Physics and Electronics, Hunan University, Changsha 410082, China

We have computed the energy loss rate (ELR) of an intruding electron in three-dimensional tilting Dirac semimetals in the light of the excitation process. In contrast to two-dimensional electron gas, ELRs contributed by single-particle excitation (ELRs$^{(SP)}$) show a nondecreasing tendency as the incidence velocity increases, and tend to replicate the behavior of the untilt intrinsic ELR$^{(SP)}$, which is described by a cubic polynomial coupling with a logarithm velocity term. In comparison, ELRs contributed by the plasmon excitation (ELRs$^{(P)}$) first reach a maximum in the small velocity region followed by a slow discrepancy. As the contribution of plasmon excitation is restricted by the vanishing imaginary part of the dielectric function, the ELRs$^{(P)}$ also manifest as an opposite counterpart to the corresponding ELRs$^{(SP)}$ with different tilts. In addition, the threshold velocities in both ELRs are tilt and chemical potential dependent, and governed by the interplay of the Pauli exclusion constraints and the conservation law concealed in the energy loss function. Finally, we briefly discuss the inelastic mean scattering time. Our results may be verified by investigating the femtosecond electron dynamics in the time-resolved two-photon photoemission.

I. INTRODUCTION

Topological materials have occupied a special place in condensed matter physics due to their nontrivial excitation spectra [1–4]. Two typical representative classes are three-dimensional (3D) Dirac semimetals (DSMs) and Weyl semimetals, both of which exhibit linear dispersing energy bands, but are distinct from each other due to their different degeneracy degrees of freedom at the zero energy points [5]. Fundamentally, the Hamiltonian of a DSM is described by only three of the Dirac matrices, giving rise to fourfold degeneracy in nature. However, there is an additional fourfold Dirac matrix that can lead to a gap opening [6]. When certain symmetry-breaking perturbations are introduced to break the inversion symmetry or the time-reversal symmetry, the fourfold degenerate Dirac nodes decouple into two sets of twofold degenerate Weyl nodes with opposite chiralities that have to be created or annihilated in pairs owing to Kramers' theorem [7]. This peculiar topological feature of Weyl nodes plays an important role in inducing the anomaly charity effect under parallel magnetic and electric fields (i.e., an Adler-Bell-Jackiw anomaly) [8,9]. Moreover, the projections of Weyl nodes on the Brillouin zone surface are manifested as the end points connecting the surface Fermi arcs [10].

A generic effective Hamiltonian of a single Dirac node can be compactly expressed as [11–16] $H(\boldsymbol{k}) = \sum_{i,j} k_i v_{ij} \sigma_j$, where $i = (x, y, z)$, $j = (0, x, y, z)$, $\boldsymbol{k}$ is the wave vector, v_{ij}'s are the velocity coefficients, and σ_j is the identity or Pauli matrix. The energy spectrum is $\varepsilon_{\pm}(\boldsymbol{k}) = \sum_i k_i v_{i0} \pm \sqrt{\sum_{j \neq 0}(\sum_i k_i v_{ij})^2} = T(\boldsymbol{k}) \pm U(\boldsymbol{k})$, where $U(\boldsymbol{k})$ is analogous to the potential and $T(\boldsymbol{k})$ denotes the kinetic term. A

finite $T(\boldsymbol{k})$ leads to tilting Dirac cones, and the values of $U(\boldsymbol{k})$ and $T(\boldsymbol{k})$ determine the degrees of the tilt. With a suitable diagonal treatment, $U(\boldsymbol{k})$ can be cast into an upper diagonal form [17,18], and a dimensionless parameter $\eta = \sqrt{\sum_{i=x,y,z}(v_{i0}/\sum_{j \neq 0} v_{ij})^2}$ can be used to describe the tilt [19]. Several remarks can be made for the case where a tilt is present. First, if η is finite, the tilting band crossing breaks the particle-hole symmetry [20,21], and beyond $\eta = 1$, the velocities of electrons in both the $\boldsymbol{k}$ and $-\boldsymbol{k}$ states bear the same sign [22]. Second, when $\eta > 1$ the low-energy fermions violate the Lorentz symmetry in the overtilted Dirac cone. Fermions of this kind can only exist in solid-state matter where the space-time that electrons experience is confined to the background crystal they are mounted on [23], and have no direct counterpart in high-energy physics [24]. Third, as $\eta > 1$ the Fermi surface at zero energy deforms as the tilt is enhanced, and eventually evolves into an open arc with a finite density of states. This key feature necessarily gives rise to the coexistence of holes and electrons below the Fermi surface [25]. Finally, it has been proposed that the flat band appearing in the critical situation of $\eta = 1$ (also known as the Lifshitz phase transition) is analogous to the black hole horizon [26,27], but this condition has not yet been experimentally synthesized in any compounds. Fundamentally, tilting DSM materials can host exotic quantum states that lead to interesting physical properties, such as anisotropic optical conductivity [28], direction-dependent chiral anomaly [29], kinked plasmon dispersion [30,31], and so on. Therefore, it is of wide interest to explore the underlying fundamental nontrivial physics in tilting DSMs further.

The energy loss rate (ELR), which is closely related to the stopping power, measures the energy dissipation along the path of a charged projectile passing through solid materials

*chenqj@hnu.edu.cn

as a consequence of collisions with nuclei and electrons of the medium [32–36]. It offers a powerful tool for exploring phonon and plasmon excitation, surface properties, and the inelastic mean free path in various systems [37–43]. Within dielectric formalism, the ELRs of a fast charge have been investigated for the whole velocity range to illustrate the physical insights of the collective modes and single-particle excitations during inelastic scattering processes in a two-dimensional electron gas (2DEG) [44–47], a marginal Fermi liquid [48], and Rashba spin-orbit coupling systems [49]. The transient readjustment of electrons in response to a swiftly moving charged particle can induce polarization and dynamic screening via Coulomb interaction, which plays an essential role in the energy degradation and angle deflection of the particle. If the intruding particle is an electron, one immediate consequence is that this electron becomes indistinguishable from those in the medium, which builds strong constraints on the scattering channels on account of Pauli blocking.

Another interesting consequence of an intruding electron is the interaction with 3D Dirac plasmons. In contrast to the gapless plasmon modes in 2D electron systems, plasmon dispersions in 3D DSMs are generally gapped [50–53]. For example, Politano *et al.* reported an experimental observation on gapped 3D plasmons in PtTe$_2$ with $\eta > 1$ (also termed as "type-II" DSMs) using high-resolution electron energy loss spectroscopy [54]. Importantly, the gap is proportional to the chemical potential or $n^{1/3}$, which affects the threshold velocity of the ELR significantly.

In this work, based on dielectric formalism, we compute the ELR of an electron passing through 3D undoped ($\mu = 0$) and doped ($\mu \neq 0$) tilting DSMs, and describe the total inelastic scattering associated with single-particle excitation (SPE), and plasmon excitation (PE). We discuss in detail the underlying excitation mechanisms, the key features of both ELR$^{(SP)}$ and ELR$^{(P)}$, as well as the corresponding threshold velocities and inelastic mean scattering times.

The rest of the paper is organized as follows. In Sec. II, we introduce a model for describing the interactions between the intruding electron and the electrons in DSMs, and outline the formalism for the ELR contributions of SPE and PE. In Secs. III and IV, we respectively discuss in detail the underlying excitation mechanisms and behaviors of ELR$^{(SP)}$ and ELR$^{(P)}$, as well as the corresponding threshold velocities. Finally, we perform a calculation on the inelastic mean scattering time in Sec. V, followed by a conclusion in Sec. VI.

II. MODEL AND FORMALISM

We consider a swift intruding electron impinging on a thin-film DSM, with the velocity being fast enough for nonadiabatic effects to be important [34], but not fast enough to approach the relativistic regime, so the electrons in the medium can respond effectively to this intruding projectile. We also ignore the phonon scattering effect [55], as we are mainly interested in the energy loss behavior due to the electron excitations in zero temperature limits. According to the first Born approximation, the traveling electron with momentum $\boldsymbol{p}$ interacts with electrons in the DSMs through the screened Coulomb interaction V_{ex-e}, and scatters to the state $\boldsymbol{p}\text{-}\boldsymbol{q}$ with a well-defined transfer momentum $\boldsymbol{q}$. The ensuing

energy loss of the intruding electron is $\Delta = \boldsymbol{q} \cdot \boldsymbol{v} - \frac{q^2}{2}$. Here, we have adopted the Hartree atomic units $\hbar = m_e = e = 1$. The Hamiltonian describing the above scenario can be written as

$$H = H_0 + H_{\text{I}}, \tag{1}$$

where H_0 is the "minimal" effective Hamiltonian of a Dirac node with fixed chirality [17,20,25]: $H_0 = v_F(\chi \eta k_z \sigma_0 + \boldsymbol{k} \cdot \boldsymbol{\sigma})$, where $\chi = \pm 1$ represents the node index, η is the tilting parameter, $\boldsymbol{\sigma} = (\sigma_x, \sigma_y, \sigma_z)$ is the 3D vector of the Pauli matrices, and the isotropic Fermi velocity $v_F = 0.65 \times 10^6$ m/s. This Hamiltonian gives the energy dispersion $\varepsilon_{\boldsymbol{k},s} = v_F(\chi \eta k_z + sk)$, with $s = \pm 1$ corresponding to the conduction and valence bands, respectively. By constructing the field operator $\Psi(\boldsymbol{r}) = \sum_{\boldsymbol{k},s} a_{\boldsymbol{k},s} \phi_{\boldsymbol{k},s} e^{i\boldsymbol{k}\cdot\boldsymbol{r}}$ and $\Psi^\dagger(\boldsymbol{r}) = \sum_{\boldsymbol{k},s} a_{\boldsymbol{k},s}^\dagger \phi_{\boldsymbol{k},s}^\star e^{i\boldsymbol{k}\cdot\boldsymbol{r}}$ [where $a_{\boldsymbol{k},s}^\dagger$ ($a_{\boldsymbol{k},s}$) is the creation (annihilation) operator for an electron in the medium, and $\phi_{\boldsymbol{k},s}$ is the eigenfunction of H_0], the Hamiltonian can be cast in the second quantized notation: $H_0 = \sum_{\boldsymbol{k},s} \varepsilon_{\boldsymbol{k},s} a_{\boldsymbol{k},s}^\dagger a_{\boldsymbol{k},s}$. It is noted that H_0 is only valid on one of the chiralities; the other is given by $H_0^\star$, which produces the same energy loss process as H_0 if we neglect the intervalley coupling. We also assume the tilt is along the k_z direction, and ignore the anisotropic in the k_x-k_y plane for simplicity. The second term H_{I} on the right-hand side of Eq. (1) represents the interaction between the external electron and the DSM electrons, which is given by [56]

$$H_{\text{I}} = \sum_{\boldsymbol{k},\boldsymbol{q},s} V_{\boldsymbol{q}} e^{-i\boldsymbol{q}\cdot\boldsymbol{R}_{\text{I}}} \phi_{\boldsymbol{k},s}^\star \phi_{\boldsymbol{k}-\boldsymbol{q},s} a_{\boldsymbol{k},s}^\dagger a_{\boldsymbol{k}-\boldsymbol{q},s}. \tag{2}$$

Here, $V_{\boldsymbol{q}}$ describes the effective screening potential between the intruding electron and the Dirac electrons, and $\boldsymbol{R}_{\text{I}}$ is the position vector of the external electron. Although the angle deflection of the incoming electron is significant and unpredictable in scattering processes where the nuclear ions are considered to be at rest, the average ELR is energy dependent. In general, the ELR of a charged particle is defined as

$$\frac{dE}{dt} = \iint d\omega \frac{d^3q}{(2\pi)^3} \omega W(\boldsymbol{q}, \omega). \tag{3}$$

Here, the transition probability function $W(\boldsymbol{q}, \omega)$ for finite temperatures is given by the Fermi's golden rule:

$$W(\boldsymbol{q}, \omega) = 2\pi \sum_{\boldsymbol{k},\boldsymbol{k}',s,s'} |\langle \boldsymbol{k}'| \langle f| H_{\text{I}} |i\rangle |\boldsymbol{k}\rangle|^2 \delta(\omega - \varepsilon_{\boldsymbol{k}',s'} + \varepsilon_{\boldsymbol{k},s}). \tag{4}$$

The interaction matrix element $\langle \boldsymbol{k}'| \langle f| H_{\text{I}} |i\rangle |\boldsymbol{k}\rangle$ describes the general two-body interaction via the Coulomb potential H_{I}. $|i\rangle$ and $|f\rangle$ are, respectively, the initial and final states of the incident electron, while $|\boldsymbol{k}\rangle$ and $|\boldsymbol{k}'\rangle$ correspond to the initial and final electron states in the DSMs. For a swift free electron, we treat $|i\rangle$ and $|f\rangle$ as plane waves, i.e., $|i\rangle = e^{i\boldsymbol{p}\cdot\boldsymbol{R}_{\text{I}}}$ and $|f\rangle = e^{i(\boldsymbol{p}-\boldsymbol{q})\cdot\boldsymbol{R}_{\text{I}}}$, respectively. Therefore, within the random phase approximation (RPA) for the dynamic polarization, the transition probability function $W(\boldsymbol{q}, \omega)$ can be cast into the form

$$W(\boldsymbol{q}, \omega) = 4\pi V_{\boldsymbol{q}} \text{Im}\left(-\frac{1}{\kappa(\boldsymbol{q}, \omega)}\right) \delta(\omega - \Delta). \tag{5}$$

It is noted that $\kappa(\boldsymbol{q}, \omega) = 1 - V_q Q(\boldsymbol{q}, \omega)$ is the dynamic dielectric function, and $V_q = \frac{4\pi}{\kappa_r q^2}$ is the 3D Coulomb potential of electron-electron interaction, with κ_r being the background static dielectric constant. The dynamic polarization function $Q(\boldsymbol{q}, \omega)$ in the bubble diagram is defined by

$$Q(\boldsymbol{q}, \omega) = \frac{g}{(2\pi)^3} \lim_{\eta \to 0} \sum_{\boldsymbol{k}, s, s'} \frac{n_{\boldsymbol{k},s} - n_{\boldsymbol{k}+\boldsymbol{q},s'}}{\varepsilon_{\boldsymbol{k},s} - \varepsilon_{\boldsymbol{k}+\boldsymbol{q},s'} + \omega + i\eta}$$
$$\times |\langle \phi_{\boldsymbol{k}+\boldsymbol{q},s'} | |\phi_{\boldsymbol{k},s}\rangle|^2, \quad (6)$$

where $g = 2$ is the valley degeneracy factor and $n_{\boldsymbol{k},s}$ is the equilibrium Fermi distribution function. The noninteraction polarization functions of the intrinsic and extrinsic parts at zero temperature were calculated analytically in [54,57].

It should also be noted that our formalism of Eq. (3) has naturally included the trapping process that the intruding particle (in state $|i\rangle$) is captured by the ion and filled to the state of ($|f\rangle = |\boldsymbol{k} \pm \boldsymbol{q}\rangle$) below the Fermi surface, since in DSMs the intruding electrons are indistinguishable from fermions. However, additional constraints should be imposed on the scattering matrix in Eq. (4) based on the following considerations. (i) We refer to swift electrons whose velocity is high enough so that the outgoing energy remains higher than the chemical potential (μ) of DSMs. That is, we exclude events where intruding electrons are trapped by the sample, which would not be observed experimentally. (ii) The electrons in the medium are not allowed to escape to the vacuum state, which imposes a limitation on the maximum transfer momentum $\boldsymbol{q}$. (iii) The energy loss is irreversible, so Δ has to be positive. Applying these constraints into Eq. (5), and substituting into Eq. (3), we can easily obtain

$$\frac{dE}{dt} = \frac{1}{\pi^2} \int_0^\pi \sin \theta_q d\theta_q \int_0^{q_+} q^2 dq \, V_q \text{Im}\left(-\frac{1}{\kappa(\boldsymbol{q}, \Delta)}\right)$$
$$\times \Delta \Theta(\Delta)[1 - \Theta(2\mu - |\boldsymbol{v} - \boldsymbol{q}|^2)]. \quad (7)$$

In the derivation of Eq. (7), we integrated over ω taking advantage of the delta function. It should be pointed out that the second aforementioned constraint is self-guaranteed within the nonzero zones of the loss function $\text{Im}[-\frac{1}{\kappa(\boldsymbol{q},\omega)}]$, whereas the positive energy loss also implies an upper limit for q_+: $q_+ = 2v$.

The energy loss function describes the probability of an excitation associated with energy ω and momentum q, and its poles define the frequency of the plasmon mode of bulk electrons. Using the identity $\lim_{\eta \to 0} \frac{1}{x \pm i\eta} = \mathscr{P}\frac{1}{x} \mp i\pi\delta(x)$, one can separate Eq. (7) into two parts on account of two different mechanisms:

$$\left(\frac{dE}{dt}\right)_{\text{SP}} = 32 v_F^4 \alpha \int_0^{q_+} dx \int_{x/2\tilde{v}}^{\min\{1, (x^2 + \tilde{v}^2 - \tilde{\mu})/2\tilde{v}x\}} d\xi$$
$$\times \frac{\tilde{\Delta} \text{Im}[\kappa(x, \tilde{\Delta})]}{[\kappa(x, 0)]^2}, \quad (8)$$

for the SPE-contributed ELR (ELR$^{(\text{SP})}$), and

$$\left(\frac{dE}{dt}\right)_{\text{P}} = 32\pi v_F^4 \alpha \int_0^{q_+} dx \int_{x/2\tilde{v}}^{\min\{1, (x^2 + \tilde{v}^2 - \tilde{\mu})/2\tilde{v}x\}} d\xi$$
$$\times \tilde{\Delta}\delta[\kappa(x, \tilde{\Delta})], \quad (9)$$

for PE-contributed ELR (ELR$^{(\text{P})}$). In the above two equations, we have used the dimensionless notations $\xi = \cos\theta_q$, $x = \frac{q}{2v_F}$, $\tilde{\Delta} = \frac{\Delta}{4v_F^2} = x\xi - \frac{x^2}{2}$, $\tilde{v} = \frac{v}{2v_F}$, $\tilde{\mu} = \frac{\mu}{4v_F^2}$, and $\alpha = \frac{1}{\pi\kappa_r v_F}$. For simplicity, in Eq. (8) the effective screening potential has been treated as static. The step functions appearing in Eq. (7) have been solved for the integration limit of ξ. For the cases of finite μ, we will compute the ELR of both types of DSMs numerically with the help of the full expressions of the dielectric function given in [54] or [57]. In addition to the step functions of Eq. (7), the integral is also restricted to run over all the nonzero zones of the imaginary part of the polarization function in the Δ-q plane [54,57]. Notably, the delta function in Eq. (9) implies the undamped PE, that is,

$$\delta[\kappa(x, \tilde{\Delta})] = \delta[\text{Re } \kappa(x, \tilde{\Delta})]\delta[\text{Im } \kappa(x, \tilde{\Delta})]. \quad (10)$$

Here, Re $\kappa(x, \tilde{\Delta})$ and Im $\kappa(x, \tilde{\Delta})$ are the real and imaginary parts of the dielectric function, respectively. Then, the integration over the region Im $\kappa(x, \tilde{\Delta}) = 0$ is regarded as the opposite counterpart to Eq. (8).

III. SINGLE-PARTICLE EXCITATION-CONTRIBUTED ENERGY LOSS RATES

A. Scattering angle and excitation mechanisms

In some experimental situations [58], the energy loss of the intruding electrons is measured via sweeping over an effective range of angles. We use the angle-resolved ELR$^{(\text{SP})}$ (AR-ELR$^{(\text{SP})}$) from Eq. (7):

$$\left(\frac{dE}{dt}\right)_{\text{SP}}(\theta) = \frac{\sin\theta_q}{\pi^2} \int_0^{q_+} q^2 dq \, V_q \text{Im}\left(-\frac{1}{\kappa(\boldsymbol{q}, \Delta)}\right)$$
$$\times \Delta\Theta(\Delta)[1 - \Theta(2\mu - |\boldsymbol{v} - \boldsymbol{q}|^2)]. \quad (11)$$

In Fig. 1, we show the numerical results of AR-ELR$^{(\text{SP})}$ as a function of the scattering angle at different tilts. For the case of $\mu = 0$ and $\eta = 0$, the scattering angle is centered at a peak of $20.7°$, with $\sim90\%$ of transmitted electrons contained in the forward direction out to $30.1°$, the upper angle of the full width half maximum (FWHM). As the tilt increases, the scattering peaks broaden and the peak maxima shift to larger angles, accompanied with higher energy loss. The underlying mechanisms can be further interpreted using the schematics depicted in Fig. 2. For instance, when the Dirac cone begins to tilt (within the range $0 < \eta < 1$), the interband dissipation path ① in Fig. 2(b) requires a larger θ_q in order to fulfill the momentum and energy conservation compared to the same path ① in the upright Dirac cone in Fig. 2(a). Upon closer inspection in Fig. 2 from (a) to (c), one can find that the tilt only acts on the band ("DA") crossing the second and fourth quadrants with the electron velocity being negative initially [see Figs. 2(a) and 2(b)]. As the tilt increases, the band "DA" rotates anticlockwise, and eventually becomes the one in Fig. 2(c), where the electrons have positive velocities. Therefore, increasing the tilts would significantly raise the probabilities of large-angle momentum transitions and the indirect ($q \neq 0$) interband transitions. This is in fact a necessary consequence of the particle-hole symmetry breakage in single Dirac cones.
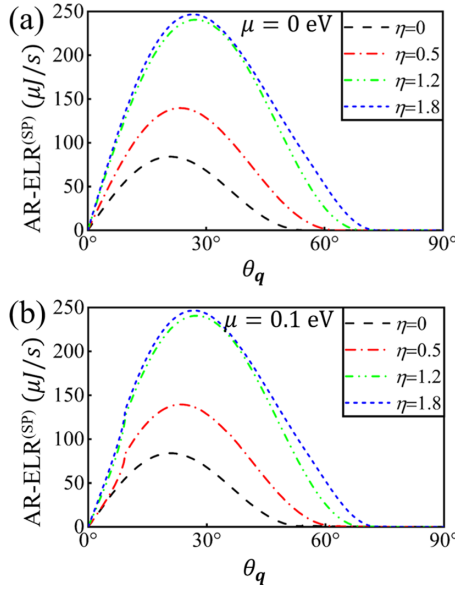
FIG. 1. AR-ELR$^{(SP)}$ due to SPE as a function of the scattering angle θ_q, with an incident velocity of about $v = 0.5$ a.u. The chemical potentials are (a) $\mu = 0$ and (b) $\mu = 0.1$ eV, respectively.
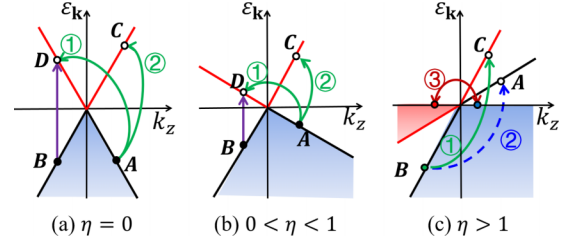

FIG. 2. Schematics for SPEs in DSMs at different tilts: (a) $\eta = 0$, (b) $0 < \eta < 1$, and (c) $\eta > 1$, respectively. For illustrative cases, we assume the tilt is along the k_z direction, and the dots represent the co-ordinates: $A = (\pm k_\parallel, k_z)$, $B = D = (\pm k_\parallel, -k_z)$, and $C = (\pm k'_\parallel, -k'_z)$, with $k_\parallel = (k_x, k_y)$. Solid and dashed lines represent interband and intraband transitions, respectively. In (a) and (b), the green paths refer to indirect transitions, whereas the purple path represents the direct transition with no need of transfer momentum. For $\eta > 1$ in (c), two additional anomalous dissipation paths, labeled as ② and ③, represent the elastic interband and large-angle intraband transitions, respectively.

On the other hand, for $\eta > 1$, apart from the normal interband transition of path ① in Fig. 2(c), two additional anomalous dissipation paths can occur via paths ② and ③. First, path ② indicates that the intraband excitation assisted by a large-angle transfer momentum $\boldsymbol{q}$ becomes permissible in the clean limit of $\mu = 0$. Such intraband transitions are not possible in a clean DSM for the lake of itinerant electrons. Second, a new type of elastic interband transition (path ③) is also permitted for electrons near the Fermi surface under infinitesimal excitations. The permission of this decay path (③) is nontrivial because it has no excitation counterpart even in doped normal DSM systems (i.e., $0 \leqslant \eta < 1$ with $\mu \neq 0$). We emphasize that both additional anomalous dissipation paths are particularly intriguing, as they are only possible in systems where electrons and holes coexist in both the valence and conduction bands. This scenario only appears when the low-energy band crossings are strongly tilted, to the extent that the Fermi surface deforms into an open Fermi arc. Looking again at Fig. 1, we notice that there is evidence of such excitation mechanisms. For the cases of $\eta = 1.2$ and $\eta = 1.8$, one can see that the peaks shift to the higher angle of $27°$ in contrast to that of $\eta = 0$. Meanwhile, the FWHMs span up to $70.2°$ and $73.4°$, respectively, which are much wider than those of $\eta < 1$, implying that the electrons are scattered at larger angles at the cost of higher energy loss.

In addition, we also note that the distribution of the scattering angle is insensitive to the chemical potential, as shown in Figs. 1(a) and 1(b). In fact, as the chemical potential is lifted to the conduction band, the intraband transitions do not contribute to the AR-ELR$^{(SP)}$ as much as they do to the onsets of the velocity threshold (see Fig. 3). This is because the intraband transition is relevant only when the excitation energy is small. In the case of high incident energy (i.e., $v = 0.5$ a.u., beyond the onsets of interband transitions marked in Fig. 3), the intraband contribution is weak, while

the interband contribution is slightly suppressed by the increasing chemical potential due to the energy conservation law ($\Delta > 2\mu$) and reduced phase space. As shown in Fig. 1(b), the tiny kinks at small angle regime suggest that the impactions of chemical potential on the distribution of scattering are minute. This is interesting because the AR-ELR$^{(SP)}$ overlooks the details of chemical potential, but still captures the information of the tilts. Thus, we suggest that the scattering angle is a relatively robust topological property that may be useful for the qualitative characterization of topological phase transition.

B. ELR$^{(SP)}$ behavior as function of v

To explore the dependence of ELR$^{(SP)}$ on incident velocity in detail, we next proceed to compute Eq. (8) explicitly in the limit of $\mu = 0$ and $\eta = 0$. The intrinsic ($\mu = 0$) imaginary dielectric function of the tilted DSM, Im $\kappa^0(x, \tilde{\Delta})$, was presented in [54,57]. Using the notations defined above, we have

$$\text{Im } \kappa^0_\chi(x, \tilde{\Delta}) = \frac{\pi \alpha}{3} \Theta(2\tilde{\Delta} + \chi \eta \xi x - x). \quad (12)$$

It is noted that, apart from the step function that imposes an additional limit on ξ: $\xi > \frac{x+1}{2\tilde{v}+\chi\eta}$, Eq. (12) is x (or equivalently, q) independent. Letting $\eta = 0$, Eq. (12) describes a 3D nontilted Dirac cone. Making use of Eq. (12) together with the static dielectric function given in [54,57], we leverage the angle integral in Eq. (8) first to obtain an expression for ELR$^{(SP)}$ of $\mu = 0$ and $\eta = 0$:

$$\left(\frac{dE}{dt} \right)_{\mu=0, \eta=0} = \frac{3\pi v_F^4}{4\tilde{v}} \int_0^{2\tilde{v}-1} dx \frac{x^3 - 4\tilde{v}x^2 + (4\tilde{v}^2 - 1)x}{\left(\ln \frac{2\tilde{\Delta}}{x} \right)^2}. \quad (13)$$

Here, $\tilde{\Lambda} = \frac{\Lambda}{4v_F^2}$ is the ultraviolet cutoff. The difficulty in solving Eq. (13) is the logarithm term in the denominator. Fortunately, with the help of a suitable expansion, we can obtain a lengthy solution that is composed of a cubic v polynomial and a logarithm term in v, as given in the Appendix.
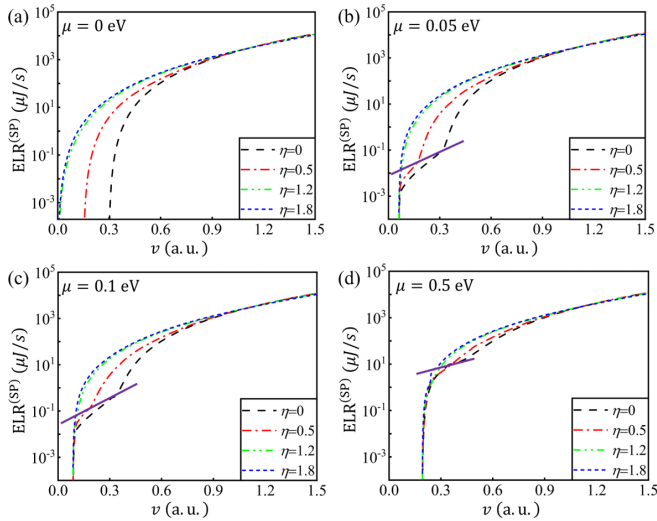
FIG. 3. Velocity dependent ELR$^{(SP)}$ of a charged particle due to the single-electron excitation with a set of tilting parameters. The chemical potentials are fixed at: (a) $\mu = 0$, (b) $\mu = 0.05$ eV, (c) $\mu = 0.1$ eV and (d) $\mu = 0.5$ eV, respecitvely. The solid purple lines cut at the onset of the interband contribution.

The behavior of ELR$^{(SP)}$ is governed by several parameters: the incidence velocity, the tilting parameter, and the chemical potential. As illustrative cases, we present in Fig. 3(a) the ELRs$^{(SP)}$ versus the incident velocity v for $\mu = 0$ and $\eta = 0$, together for $\eta = 0.5$, 1.2, and 1.8. In the high incident velocity region, v dependence is dominated by the cubic polynomial term, whereas in the low incident velocity region, the ELRs$^{(SP)}$ are determined by a cubic v polynomial coupled with a logarithmic v term [see Eq. (A2) in the Appendix], which endows ELRs$^{(SP)}$ with a nondecreasing v dependence behavior strikingly different from those of parabolic electron systems [58–60]. In parabolic electron systems such as those in [59] and [60], the ELRs$^{(SP)}$ generally reach a maximum and then decrease as the incidence velocity increases. However, the nondecreasing behavior of ELRs$^{(SP)}$ in the DSMs arises entirely from the fundamental nature of the linear excitation spectrum and the high Fermi velocity of the massless Dirac fermions, which subsequently give rise to a dielectric behavior fundamentally different from that of parabolic electron systems. For example, the polarization of the ordinary 2DEG decreases with an increasing wave vector for $q > 2k_F$, whereas the intrinsic imaginary dielectric function of 3D DSMs with $\eta = 0$ does not contain q [61]. As a result, the latter contributes to the integral in Eq. (8) continuously as v goes beyond $2v - 1 > 2\mu$, leading to the nondecreasing behavior of ELRs$^{(SP)}$. In fact, a similar v dependency of ELRs has been previously reported in graphene [46]. However, our results associated with the Dirac cones in 3D nature are substantially different from that of a perfect 2D graphene, in which the intrinsic imaginary dielectric function is linear in q. Thus, one can expect a much more dramatic ELR increase with v in graphene [46].

In addition, it is straightforward to see that the curves with different tilts will eventually converge to the case of $\eta = 0$ in the region of high v. This is somewhat interesting as it implies

that a swift intruding electron can strongly interact with the medium Dirac electrons but ignore the tilting details of the Dirac cones. However, it should not be surprising that, under a high energy excitation, the information of the tilt is washed out by the averaging treatment, provided that the topological phase transition due to the tilt is also a Fermi liquid property that is typically described by models of effective low-energy bands near the Fermi surface.

Tilting DSMs with finite μ, as plotted in Figs. 3(b)–3(d), contain all the energy loss information as that of $\mu = 0$ in the high v region, while in the region where v is small, two interesting remarks are in order. (i) The intraband SPE begins to contribute, as indicated by the solid purple lines in Figs. 3(b)–3(d), which cuts through all the turning points. Below these turning points, the ELRs$^{(SP)}$ are solely contributed by the intraband SPE. (ii) The threshold velocity becomes a function of μ only, since the intraband SPE removes the excitation barrier for the interband transition. We will discuss the threshold velocity further in the next section.

C. Threshold velocity

Another feature observed in Fig. 3 is that the ELRs$^{(SP)}$ of a penetrating electron begin with different threshold velocities related to the tilting strength. In particular, for the case of $\mu = 0$ and $0 \leqslant \eta < 1$, the threshold velocities are proportional to η. For instance, the threshold velocities are about $v_{th} \approx 0.30$ a.u. and $v_{th} \approx 0.16$ a.u. for $\eta = 0$ and $\eta = 0.5$, respectively. Essentially, this state of affairs arises from the imaginary part of the dielectric function. With a simple manipulation on the step function in Eq. (12), we can obtain an expression for the maximum transfer momentum x_m (or $q_m/2v_F$):

$$x_m = (2\tilde{v}\xi - v_0), \qquad (14)$$

with $v_0 = 1 - \eta\xi$ being a material-dependent parameter. To ensure $x_m > 0$, the incident velocity must lie above the parameter v_0, corresponding to the onset velocity in Fig. 3(a). Physically, this condition is necessarily required by the energy and momentum conservation laws for the particle-hole transition in a general two-body scattering process, so for the cases of $x_m < 0$ or $v < v_0$, scattering via a single-electron process is forbidden. On the other hand, if $\eta > 1$, the maximum transfer momentum x_m always picks up a positive value for arbitrary $\tilde{v}$ (or v). As such, the ELRs$^{(SP)}$ appear with any infinitesimal incident velocity, as illustrated by the $\eta = 1.2$ and 1.8 curves in Fig. 3(a). As a matter of fact, the threshold velocity of $\mu = 0$ simply corresponds to the onset of the interband SPE, whereas in the cases of $\mu > 0$, the intraband SPE contributes to the low-energy excitation. In this case, one should take into account the condition of $[1 - \Theta(2\mu - |\boldsymbol{v} - \boldsymbol{q}|^2)]$, which suggests all the scattering events with incident velocity below $\sqrt{2\mu}$ are canceled by the term $\Theta(2\mu - |\boldsymbol{v} - \boldsymbol{q}|^2)$. Equivalently, the intraband SPE contribution has to be excluded if the incident energy is below μ. This is also required by the assumption that the intruding electron is not reflected.
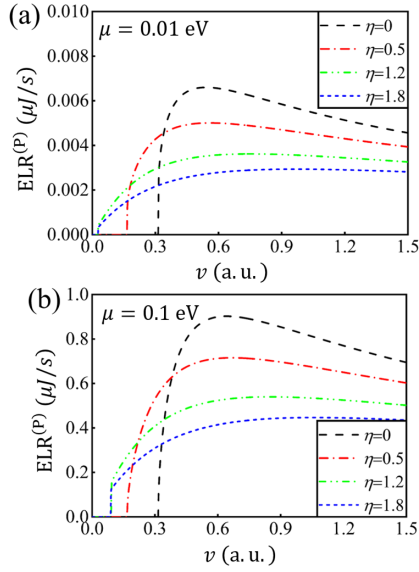
FIG. 4. ELR$^{(P)}$ originating from plasmon as a function of incident velocity for different tilting parameters.

IV. PLASMON EXCITATION CONTRIBUTION TO ENERGY LOSS RATES

In the intrinsic limit, the system does not allow bulk PE due to the lake of free carries supporting the self-sustaining in-phase density oscillations [62]. Hence, we focus on the plasmon-contributed ELR (ELR$^{(P)}$) of an electron to the DSM systems of finite μ. In the long wave approximation, the approximate expression for plasmon dispersion has the form [57]

$$\omega_{pl} \approx \Delta_{pl}(1 - Dx^2) + x\eta\xi. \tag{15}$$

Here, Δ_{pl} is defined following Eq. (3) of [54], capturing the plasmon gap at $q = 0$, and can be solved self-consistently. We note that Δ_{pl} is linear in μ. The factor D is equal to $-\frac{1}{8\tilde{\mu}^2}[1 + G(2\tilde{\mu}, \Delta_{pl})]$ with $G(z_1, z_2) = \frac{z_1^4(z_2^2 - \frac{3}{5}z_1^2)}{z_2^2(z_1^2 - z_2^2)^2}$. To calculate Eq. (9), it is convenient to define a modified frequency $y \equiv \omega_\chi = \tilde{\Delta} + x\eta\xi$, and change the integral variable ξ to y, followed with $dy = (1 + \frac{\eta}{2})x \, d\xi$. Making use of Eq. (15) and integrating over y, we achieve a simpler form for ELR$^{(P)}$:

$$\left(\frac{dE}{dt}\right)_P = \frac{32v_F^4\alpha\pi}{(2\tilde{v} + \eta)^2} \int_0^{q_+} dx(4\tilde{v}y_0 - \eta x^2)\Theta(2y_0 - x)$$
$$\times \frac{\Theta(\min[\Omega_1(x), \Omega_2(x), \Omega_3(x)] - y_0)}{x|\partial_y\kappa(x, y)|_{y=y_0}}. \tag{16}$$

Here, $y_0 = \Delta_{pl}(1 - Dx^2)$ is the modified plasmon frequency. $\Omega_1(x) = 2\tilde{\mu} - x/2$ and $\Omega_2(x) = (\tilde{v} + \eta/2) - x^2/2$ are extracted from Im $\kappa(x, y) = 0$ and the natural condition $\xi < 1$, respectively, whereas $\Omega_3(x) = (2\tilde{v} + \eta)(\tilde{v}^2 + x^2 - \tilde{\mu})/4\tilde{v} - x^2/2$ is the by-product of the first integral. The step functions will play critical roles in determining the threshold velocity.

A. ELR$^{(P)}$ behavior

The PE-contributed ELRs were evaluated numerically using Eq. (16), and are plotted in Fig. 4 as a function of incident

velocity for $\mu = 0.01$ and 0.1 eV, respectively. In contrast to the nondecreasing behavior of ELR$^{(SP)}$, all ELRs$^{(P)}$ first reach a maximum and then decrease slowly with v, which is a tendency similar to the ELR in the 2DEG [60]. In fact, within the Lindhard formalism, the information of the undamped plasmon is accessible only for rather restricted ranges of the arguments (q, Δ). As long as the plasmon resonance peaks cross the boundary of the particle-hole continuum, the plasmon contribution vanishes due to the bulk-electron excitation damping into the SPE. However, the region of Im $\kappa(x, y) = 0$, where the plasmon mode is sustained, can be strongly modified by the tilt (i.e., region 1B in Fig. 1 of [31]). This is partially the reason that the ELR$^{(P)}$ drops as the tilt is enhanced. Additionally, as Eq. (15) suggests, the tilting parameter will also push the plasmon mode to higher energies, further limiting its contribution to the ELR$^{(P)}$. Therefore, for a given chemical potential, the discrepancy of the ELR$^{(P)}$ with tilt can be regarded as the opposite counterpart to the enhancement of the ELR due to the SPE. Finally, we should also point out that for a given value of η, the ELR$^{(P)}$ is enhanced if the chemical potential is raised. However, this is not surprising if one observes Eq. (15), in which the plasmon frequency is roughly proportional to μ.

B. Threshold velocity

To determine the threshold velocity, we should take the $x \to 0$ limit for the terms in the step function $\Theta(\min[\Omega_1(x), \Omega_2(x), \Omega_3(x)] - y_0)$ in Eq. (16), since the modified frequency y_0 is quadratically dependent on x and varies much more slowly than $\Omega_i(x)$ at this limit. Obviously, $\Omega_1(x)$ is always larger than $\Omega_2(x)$ and $\Omega_3(x)$ as $x \to 0$. In addition, as discussed above, the assumption of a "fast intruding electron" gives rise to the condition $v_{th} > \sqrt{2\mu}$. If this condition is guaranteed, we will have $\Omega_3(x) > \Omega_2(x) \to 0$. Then, the step function is reduced to the inequality $\Omega_2(x) < y_0$, which gives rise to the second condition for the threshold velocity:

$$v_{th} > \sqrt{2\Delta_{pl}(1 - 2D)} - \frac{\eta}{2}. \tag{17}$$

Compactly, the threshold velocity in ELRs$^{(P)}$ can be summarized as

$$v_{th} = \max\left[\sqrt{2\tilde{\mu}}, \sqrt{2\Delta_{pl}(1 - 2D)} - \frac{\eta}{2}\right]. \tag{18}$$

Although the plasmon gap is μ dependent, it is approximately one order of magnitude smaller than μ, and thus, the term $2\sqrt{\Delta_{pl}(1 - 2D)}$ is approximately equal to 1. In this situation, when $\eta < 1$, the tilt is the dominant contribution. Otherwise, the velocity threshold is determined by the chemical potential. As one can see in Fig. 4(a), the threshold velocities are $v_{th} = \sqrt{2\Delta_{pl}(1 - 2D)} - \eta/2 \approx 0.1653$ a.u. for $\eta = 0.5$ and $v_{th} = \sqrt{2\mu} \approx 0.027$ a.u. for both $\eta = 1.2$ and $\eta = 1.8$.

V. INELASTIC MEAN SCATTERING TIME

In this section, we discuss briefly the inelastic mean scattering time τ. Generally speaking, the inelastic scattering time plays an important role in investigating electronic relaxation processes and the femtosecond electron dynamics at solid
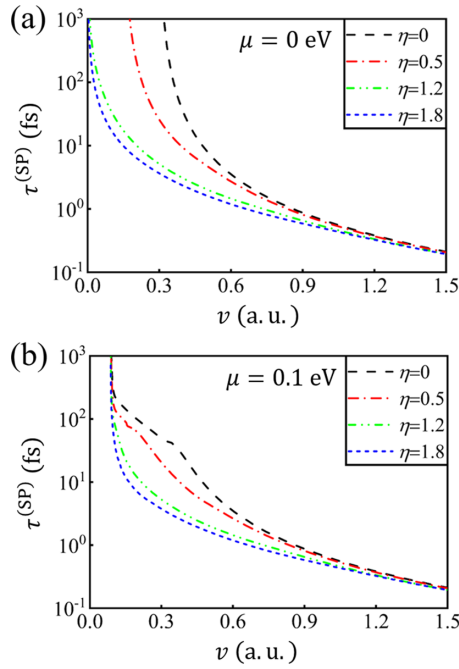
FIG. 5. Inelastic mean scattering time contributed by particle-hole transitions as a function of incidence velocity at different chemical potentials.

FIG. 6. Inelastic mean scattering time contributed by plasmon as a function of incident velocity at different chemical potentials.

surfaces [38,63], and it can be evaluated using the definition [56]

$$\frac{1}{\tau} = \int \frac{d^3q\, d\omega}{(2\pi)^3} W(\boldsymbol{q}, \omega). \tag{19}$$

In an approximate treatment, Eq. (19) can be cast into a more compendious form: $\tau = \frac{E_v}{d(E_v)/dt}$ [46,47,49]. Then, one can expect that the inelastic mean scattering times retain the detailed physics as those of the corresponding ELRs. In Figs. 5 and 6, we present the numerical results of the inelastic mean scattering time as a function of incident velocity. $\tau^{(SP)}$ and $\tau^{(P)}$ correspond to the inelastic mean scattering time related to the SPE and PE scattering paths, respectively. The initial drops from infinite in the inelastic mean scattering time reflect the fact that the quasiparticle lifetime due to electron-electron interactions near the Fermi surface is infinite within the Born approximation at $T = 0$ [64,65].

In Figs. 5(a) and 5(b), we see that, in the region of v below 0.6 a.u., $\tau^{(SP)}$ varies from a few femtoseconds to hundreds of femtoseconds for both cases of $\mu = 0$ and 0.1 eV. Although the neglect of surface-excitation effects and the plasmon broadening may lead to an overestimation of the inelastic lifetime [62], our results for the $\eta = 0$ case quantitatively match the values reported for periodically rippled graphene [63], in which the lifetimes of single graphene layers on Ru(0001) measured using time-resolved two-photon photoemission (2PPE) range from 10 to 85 fs, with energies lying in the range from 0.9 to 4.7 eV [63]. Therefore, our results may be verified by studying femtosecond electron dynamics using 2PPE. Moreover, such a wide range of variation in $\tau^{(SP)}$ is sensitive to the chemical potential only in the regions where intraband SPE contributes. On the other hand, $\tau^{(P)}$ is remarkably dependent on the chemical potential. For $\mu = 0.01$ eV,
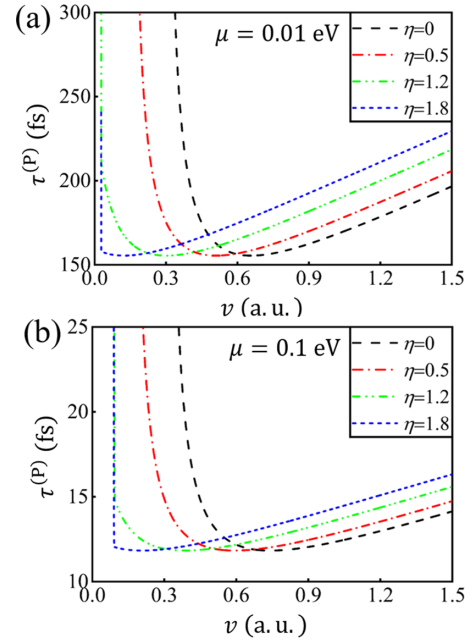
the values of $\tau^{(P)}$ are about 150–250 fs, varying slightly for the four types of tilts [see Fig. 6(a)], whereas they are significantly reduced to about 10–15 fs as the chemical potential is raised to 0.1 eV [Fig. 6(b)].

VI. CONCLUSION

In this work, the ELRs of a fast intruding electron in tilting 3D DSMs were calculated based on the excitation process within the RPA dielectric formalism. The inelastic scattering angle of SPE is dominated by small-angle scattering. The maximum scattering peaks are broadened with tilt due to the particle-hole symmetry breakage and the emergence of versatile dissipation channels, raising the probabilities of large-momentum intra- and interband transitions. In striking contrast with those in parabolic electron systems, the ELRs$^{(SP)}$ exhibit a nondecreasing v-dependent behavior due to the fact that the imaginary part of the dielectric function contains $\boldsymbol{q}$-independent terms. In the high incident velocity limit, ELRs$^{(SP)}$ with different tilts reduce to those of untilted intrinsic DSMs, which is described by a cubic polynomial and a logarithmic v term. On the other hand, the ELRs$^{(P)}$ first reach a maximum and then decrease slowly as v. Because the tilts will push the plasmon mode to higher frequencies, the ELRs$^{(P)}$ show discrepancy as the tilts are enhanced and manifest as an opposite counterpart to ELRs$^{(SP)}$. The threshold velocities are strongly dependent on the tilt and chemical potential. As tilts vary, the threshold velocities are mainly determined by the interplay of the Pauli exclusion constraints and conservation laws concealed in the energy loss function. Finally, we perform a numerical calculation on the inelastic scattering times. Within the first Born approximation, the inelastic scattering times in tilting DSMs are estimated to range from a few femtoseconds up to hundreds of femtoseconds with respect to tilt.
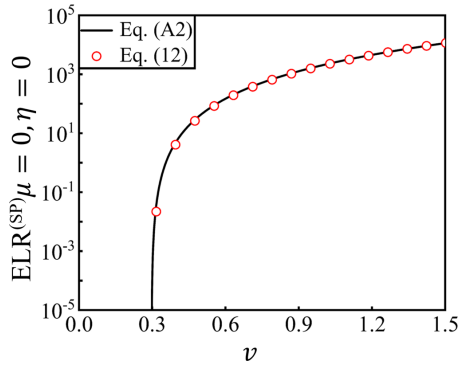
FIG. 7. Numerical result of Eq. (13) (empty red circle) and the analytical plot of Eq. (A2) (solid black line).

APPENDIX

To solve Eq. (13), we make use of the expansion for $\ln t$:

$$\ln t = 2\left[\frac{t-1}{t+1} + \frac{1}{2}\left(\frac{t-1}{t+1}\right)^2 + \cdots\right], \qquad t > 0. \quad \text{(A1)}$$

Here, we have $t = 2\tilde{\Lambda}/x \gg 1$. The main contribution to the integral is the large limit of t, in which case $\frac{t-1}{t+1} \sim 1$. Therefore, we replace $\ln t$ with the first order approximation of Eq. (A1). After integrating in Eq. (13), we obtain a lengthy expression for the ELR$^{(SP)}$ at $\mu = 0$ and $\eta = 0$:

$$
\begin{aligned}
\left(\frac{dE}{dt}\right)_{\mu=0,\eta=0} = \frac{3\pi v_F^4}{16(A-1)^2\tilde{v}}\Bigg\{ & \frac{2\tilde{v}-1}{12}[8\tilde{v}^3 + 4(9-8B)\tilde{v}^2 \\
& - 2(27 - 88B + 66B^2)\tilde{v} \\
& + 2B(14 + 33B - 30B^2) - 31] \\
& + (B-1)[4(3B-1)\tilde{v}^2 + 8B(2B-1)\tilde{v} \\
& + 5B^3 - 3B^2 - 3B + 1]\ln\left|\frac{B+2\tilde{v}-1}{B}\right|\Bigg\},
\end{aligned}
$$

(A2)

where $B = (A+1)/(A-1)$ and $A = \ln 2\tilde{\Lambda}/2$. The logarithm in the last term can be expanded again using Eq. (A1), and the corresponding results imply that the leading order in $\tilde{v}$ is cubic. To verify our analytical solution, we present the numerical result of Eq. (13) and the analytical plot of Eq. (A2) in Fig. 7. The two solutions are in perfect agreement.

[1] Y. B. Zhang, Y.-W. Tan, H. L. Stormer, and P. Kim, Nature (London) **438**, 201 (2005).

[2] X. G. Wan, A. M. Turner, A. Vishwanath, and S. Y. Savrasov, Phys. Rev. B **83**, 205101 (2011).

[3] A. A. Burkov and L. Balents, Phys. Rev. Lett. **107**, 127205 (2011).

[4] M. Neupane, S.-Y. Xu, R. Sankar, N. Alidoust, G. Bian, C. Liu, I. Belopolski, T.-R. Chang, H.-T. Jeng, H. Lin, A. Bansil, F. C. Chou, and M. Z. Hasan, Nat. Commun. **5**, 3786 (2014).

[5] P. B. Pal, Am. J. Phys. **79**, 485 (2011).

[6] S. M. Young, S. Zaheer, J. C. Y. Teo, C. L. Kane, E. J. Mele, and A. M. Rappe, Phys. Rev. Lett. **108**, 140405 (2012).

[7] P.-J. Guo, H.-C. Yang, K. Liu, and Z.-Y. Lu, Phys. Rev. B **95**, 155112 (2017).

[8] S. L. Adler, Phys. Rev. **177**, 2426 (1969).

[9] J. S. Bell and R. Jackiw, Nuovo Cimento A **60**, 47 (1969).

[10] K. Deng, G. L. Wan, P. Deng, K. N. Zhang, S. J. Ding, E. Y. Wang, M. Z. Yan, H. Q. Huang, H. Y. Zhang, Z. L. Xu, J. Denlinger, A. Fedorov, H. T. Yang, W. H. Duan, H. Yao, Y. Wu, S. S. Fan, H. J. Zhang, X. Chen, and S. Y. Zhou, Nat. Phys. **12**, 1105 (2016).

[11] A. A. Soluyanov, D. Gresch, Z. J. Wang, Q. S. Wu, M. Troyer, X. Dai, and B. A. Bernevig, Nature (London) **527**, 495 (2015).

[12] Z.-M. Yu, Y. G. Yao, and S. Y. A. Yang, Phys. Rev. Lett. **117**, 077202 (2016).

[13] M. Z. Yan, H. Q. Huang, K. N. Zhang, E. Y. Wang, W. Yao, K. Deng, G. L. Wan, H. Y. Zhang, M. Arita, H. T. Yang, Z. Sun, H. Yao, Y. Wu, S. S. Fan, W. H. Duan, and S. Y. Zhou, Nat. Commun. **8**, 257 (2017).

[14] H.-J. Noh, J. Jeong, E.-J. Cho, K. Kim, B. I. Min, and B.-G. Park, Phys. Rev. Lett. **119**, 016401 (2017).

[15] Z. Jalali-Mola and S. A. Jafari, Phys. Rev. B **102**, 245148 (2020).

[16] B. Q. Lv, T. Qian, and H. Ding, Rev. Mod. Phys. **93**, 025002 (2021).

[17] M. O. Goerbig, J.-N. Fuchs, G. Montambaux, and F. Piéchon, Phys. Rev. B **78**, 045415 (2008).

[18] G. G. Pyrialakos, N. S. Nye, N. V. Kantartzis, and D. N. Christodoulides, Phys. Rev. Lett. **119**, 113901 (2017).

[19] J. Sári, C. Tőke, and M. O. Goerbig, Phys. Rev. B **90**, 155446 (2014).

[20] M. Trescher, B. Sbierski, P. W. Brouwer, and E. J. Bergholtz, Phys. Rev. B **91**, 115135 (2015).

[21] S. Ahn, E. J. Mele, and H. K. Min, Phys. Rev. B **95**, 161112(R) (2017).

[22] T.-R. Chang, S.-Y. Xu, D. S. Sanchez, W.-F. Tsai, S.-M. Huang, G. Chang, C.-H. Hsu, G. Bian, I. Belopolski, Z.-M. Yu, S. A. Yang, T. Neupert, H.-T. Jeng, H. Lin, and M. Z. Hasan, Phys. Rev. Lett. **119**, 026404 (2017).

[23] S. A. Jafari, Phys. Rev. B **100**, 045144 (2019).

[24] H. Q. Huang, K.-H. Jin, and F. Liu, Phys. Rev. B **98**, 121110(R) (2018).

[25] K. Sadhukhan, A. Politano, and A. Agarwal, Phys. Rev. Lett. **124**, 046803 (2020).

[26] G. E. Volovik, JETP Lett. **104**, 645 (2016).

[27] G. E. Volovik, Phys.-Usp. **61**, 89 (2018).

[28] T. Nishine, A. Kobayashi, and Y. Suzumura, J. Phys. Soc. Jpn. **79**, 114715 (2010).

[29] M. Udagawa and E. J. Bergholtz, Phys. Rev. Lett. **117**, 086401 (2016).

[30] Z. Jalali-Mola and S. A. Jafari, Phys. Rev. B **98**, 195415 (2018).

[31] Z. Jalali-Mola and S. A. Jafari, Phys. Rev. B **98**, 235430 (2018).

[32] D. Goebl, K. Khalal-Kouache, D. Roth, E. Steinbauer, and P. Bauer, Phys. Rev. A **88**, 032901 (2013).

[33] R. Ullah, F. Corsetti, D. Sánchez-Portal, and E. Artacho, Phys. Rev. B **91**, 125203 (2015).

[34] J. Halliday and E. Artacho, Phys. Rev. B **100**, 104112 (2019).

[35] C.-K. Li, S. Liu, Q. Cao, F. Wang, X.-P. Ou Yang, and F.-S. Zhang, Phys. Rev. A **100**, 052707 (2019).

[36] I. Maliyov, J.-P. Crocombette, and F. Bruneval, Phys. Rev. B **101**, 035136 (2020).

[37] C. Auth, A. Mertens, H. Winter, and A. Borisov, Phys. Rev. Lett. **81**, 4831 (1998).

[38] H. T. Nguyen-Truong, Appl. Phys. Lett. **108**, 172901 (2016).

[39] T. Ogawa, S. Kobayashi, M. Wada, C. A. J. Fisher, A. Kuwabara, T. Kato, M. Yoshiya, S. Kitaoka, and H. Moriwake, Phys. Rev. B **93**, 201107(R) (2016).

[40] H. Lourenço-Martins and M. Kociak, Phys. Rev. X **7**, 041059 (2017).

[41] S.-I. Tanaka, K. Mukai, and J. Yoshinobu, Phys. Rev. B **95**, 165408 (2017).

[42] G. Chiarello, J. Hofmann, Z. L. Li, V. Fabio, L. W. Guo, X. L. Chen, S. Das Sarma, and A. Politano, Phys. Rev. B **99**, 121401(R) (2019).

[43] H. B. Yang, E. L. Garfunkel, and P. E. Batson, Phys. Rev. B **102**, 205427 (2020).

[44] N. R. Arista, Phys. Rev. B **18**, 1 (1978).

[45] C. Zhang, N. Tzoar, and P. M. Platzman, Phys. Rev. B **37**, 7326 (1988).

[46] Y. S. Ang, C. Zhang, and C. Y. Kee, Appl. Phys. Lett. **99**, 053111 (2011).

[47] Q. J. Chen, Y. S. Ang, X. L. Wang, R. A. Lewis, and C. Zhang, Appl. Phys. Lett. **103**, 192107 (2013).

[48] C. Zhang and Y. Takahashi, Phys. Rev. B **46**, 9247 (1992).

[49] W. Feng, A. Tawfiq, J. C. Cao, and C. Zhang, Appl. Phys. Lett. **102**, 052113 (2013).

[50] M. Lv and S. C. Zhang, Int. J. Mod. Phys. B **27**, 1350177 (2013).

[51] A. Thakur, R. Sachdeva, and A. Agarwal, J. Phys.: Condens. Matter **29**, 105701 (2017).

[52] R. Sachdeva, A. Thakur, G. Vignale, and A. Agarwal, Phys. Rev. B **91**, 205426 (2015).

[53] A. Thakur, K. Sadhukhan, and A. Agarwal, Phys. Rev. B **97**, 035403 (2018).

[54] A. Politano, G. Chiarello, B. Ghosh, K. Sadhukhan, C.-N. Kuo, C. S. Lue, V. Pellegrini, and A. Agarwal, Phys. Rev. Lett. **121**, 086804 (2018).

[55] At finite temperature, the thermalization process is dominated by small momentum transfers. Thus, the phonon scattering effect is important only when the external electron is cooled down to the energy scale of Fermi energy ε_F or $\sim k_B T$. This means that the inelastic electron scattering is dominated at the initial stage (before the energy decays to ε_F or $\sim k_B T$). At the final stage, the phonon scattering will come into play and has consequences on the intruding depth [R. M. Nieminen and J. Oliva, Phys. Rev. B **22**, 2226 (1980)]. Our model remains valid at finite temperature if we assumed that the external electron is swift enough to penetrate the sample (i.e., a thin film), as imposed by the constraint (i). In addition, at low temperature, the phonon scattering time is remarkably longer than the inelastic electron scattering time. For example, in Weyl semimetal WP$_2$ with $\mu = 0.01$ eV at 50 K, the phonon-electron lifetime measured by Raman spectroscopy is about 100 ps [G. B. Osterhoudt, Y. Wang, C. A. C. Garcia, V. M. Plisson, J. Gooth, C. Felser, P. Narang, and K. S. Burch, Phys. Rev. X **11**, 011017 (2021)], which is about three orders of magnitude higher than those obtained in our numerical calculation in Sec. V.

[56] P. M. Echenique, F. Flores, and R. H. Ritchie, Solid State Phys. **43**, 229 (1990).

[57] J. H. Zhou, H.-R. Chang, and D. Xiao, Phys. Rev. B **91**, 035114 (2015).

[58] W. N. Lennard, G. R. Massoumi, P. J. Schultz, P. J. Simpson, and G. C. Aers, Phys. Rev. Lett. **74**, 3947 (1995).

[59] I. Nagy, Phys. Rev. B **51**, 77 (1995).

[60] A. Bergara, I. Nagy, and P. M. Echenique, Phys. Rev. B **55**, 12864 (1997).

[61] B. Wunsch, T. Stauber, F. Sols, and F. Guinea, New J. Phys. **8**, 318 (2006).

[62] S. Das Sarma and E. H. Hwang, Phys. Rev. Lett. **102**, 206412 (2009).

[63] N. Armbrust, J. Güdde, P. Jakob, and U. Höfer, Phys. Rev. Lett. **108**, 056801 (2012).

[64] V. M. Silkin, E. V. Chulkov, and P. M. Echenique, Phys. Rev. B **68**, 205106 (2003).

[65] E. H. Hwang, Ben Yu-Kuang Hu, and S. Das Sarma, Phys. Rev. B **76**, 115434 (2007).